Fabrication and characterizations of nitrogen-doped $BaSi_2$ epitaxial films grown by molecular beam epitaxy

doi: 10.1016/j.jcrysgro.2017.05.003

Fabrication and characterizations of nitrogen-doped $BaSi_2$ epitaxial films grown by molecular beam epitaxy

Zhihao Xu[a], Tianguo Deng[a], Ryota Takabe[a], Kaoru Toko[a], Takashi Suemasu[a,*]

[a]*Institute of Applied Physics, Graduate School of Pure and Applied Sciences, University of Tsukuba, Tsukuba, Ibaraki 305-8573, Japan*

Nitrogen doped $BaSi_2$ layers are grown on high-resistivity n-Si (111) substrates by molecular beam epitaxy using a radio-frequency nitrogen plasma. The nitrogen concentration measured by secondary ion mass spectrometry is homogeneous throughout the grown layers. The carrier concentration is measured by Hall measurement using the van der Pauw method. Nitrogen-doped $BaSi_2$ shows n- or p-type conductivity, depending on the intensity of nitrogen plasma. The hole concentration is of the order of 10^{16}–10^{17} cm^{-3} at room temperature. The acceptor level is estimated to be approximately 64 meV from the temperature dependence of hole concentration. The temperature dependence of resistivity is explained by variable-range hopping conduction in p-$BaSi_2$. First-principle calculation suggests that the nitrogen atoms are most likely to occupy the interstitial site in $BaSi_2$.

Keywords: A3. Molecular beam epitaxy, A1. Impurities, B2. Semiconducting silicon compounds, B3. Solar cells

* Corresponding author at:

Institute of Applied Physics, Faculty of Pure and Applied Sciences, University of Tsukuba, Tsukuba, Ibaraki 305-8573, Japan

Electronic mail: suemasu@bk.tsukuba.ac.jp

1. Introduction

Thin-film solar cell materials such as cadmium telluride and chalcopyrite have attracted more and more attention over the last few years, because of their high efficiency and low cost [1-4]. Perovskite solar cells are also attracting increasing attention owing to their high conversion efficiency exceeding 20% and simple fabrication process [5,6]. However, these cells contain expensive and/or toxic elements. As an alternative, we have focused on the semiconductor barium disilicide ($BaSi_2$), which consists of only abundant elements [7,8]. $BaSi_2$ has many attractive features for thin-film solar cell applications from the view point of the band gap (ca. 1.3 eV), high absorption coefficients comparable to chalcopyrites, inactive grain boundaries, superior minority-carrier diffusion length and lifetime [9-11]. Very recently, we achieved a conversion efficiency approaching 10% with p-$BaSi_2$/n-Si heterojunction solar cells [12-14]. Other types of solar cells such as $BaSi_2$ nanowires and $BaSi_2$/perovskite stacked layers have also been proposed [15,16]

Towards $BaSi_2$ homojunction solar cells, control of the conductivity of $BaSi_2$ by impurity doping is a requirement. There have been several experiments on impurity-doped $BaSi_2$; $BaSi_2$ films doped with a group 13 (15) element such as B, Al, or In (As, P, or Sb) show p- (n-) type conductivity [17-22]. As for p-$BaSi_2$, hole concentrations can only be controlled over a wide range between 10^{16} and 10^{20} cm^{-3} by B doping. In contrast, electron concentrations can be controlled over a relatively wide range by P or Sb doping. These results are understood as follows. The valence band maximum of $BaSi_2$ consists mainly of the Si *p* states from hard x-ray photoelectron spectroscopy [23] and first-principle calculations [24-28]. According to theoretical calculations, substitution of Si in the $BaSi_2$ lattice is more favorable than substitution of Ba, from an energetic point of view [29]. Hence, the replacement of some Si atoms in $BaSi_2$ by a group 13 (15) element decreases (increases) the valence electron concentration and causes $BaSi_2$ to become a p- (n-) type semiconductor. The conductivity type of impurity-doped $BaSi_2$ is well estimated by the calculated position of the Fermi level, E_F

[11,29]. However, there has been no study about nitrogen (N) doped $BaSi_2$. N is a group 15 element. In crystalline Si, N is not used as a dopant because it induces deep levels in the forbidden band gap [30-32]. In this paper, we grew N-doped $BaSi_2$ films on Si(111) substrates by molecular beam epitaxy (MBE), and investigated the electrical properties of the films. First-principle calculations were also performed to find the position of the E_F, and which site the N atom is most likely to occupy in the lattice.

2. Experiment

2.1 Formation of N-doped $BaSi_2$ films

An ion-pumped MBE system equipped with a standard Knudsen cell for Ba, an electron-beam evaporation source for Si, and a radio-frequency (RF) high-purity (6N) N_2 plasma was used. High-resistivity float-zone (FZ) n-type Si (111) substrates (resistivity ρ > 1000 Ωcm) were used. After thermal cleaning of the substrate, we first deposited Ba on the Si (111) substrate at 500 °C to form a 5 nm-thick $BaSi_2$ template layer by reactive deposition epitaxy. The template works as seeds for controlling the crystal orientation of $BaSi_2$ overlayers [33]. Next, we codeposited Ba and Si on the template at 580 °C with the simultaneous supply of N source for 2 h to form N-doped $BaSi_2$ by MBE. After MBE growth, approximately 3 nm-thick amorphous Si was deposited on the $BaSi_2$ films to prevent oxidization [34]. During the MBE growth, the RF power was set to 50 or 70 W. Figure 1 shows examples of the emission spectra of nitrogen plasma obtained at 50 and 70 W, measured by a spectrometer (QE Pro; Ocean Optics). In the nitrogen plasma, many kinds of species exist, such as 1st excited neutral N_2, higher excited neutral N_2, N_2^+ ions, atomic N and so on. There are three regions in the spectrum. According to Ref. [35], the emissions in the wavelength λ ranging from 700 to 800 nm correspond to the atomic N. Among them, we used the emission intensity at λ = 746 nm, I_N, as a measure of the supply of atomic N, and varied I_N from 420 to 1100 counts. Nitrogen ions were eliminated by applying bias voltages to the plasma generator. Sample preparation

details are shown in Table 1.

The crystalline quality of grown films was characterized by reflection high-energy electron diffraction (RHEED) along the Si[$11\bar{2}$] azimuth, and X-ray diffraction (XRD) using Cu Kα radiation. A Ge (220) single crystal was used to make the incident X-rays monochromatic. We measured ω-scan X-ray rocking curves to obtain full width at half maximum (FWHM) of a $BaSi_2$ (600) diffraction peak intensity to represent its crystal quality. The electrical properties of N-doped $BaSi_2$ were measured by Hall measurement using the van der Pauw method with an applied magnetic field of 0.70 T. The temperature dependences of carrier concentration and mobility were measured using a closed-cycle He cryostat. The depth profile of N atoms was characterized by secondary ion mass spectrometry (SIMS) using O_2^- ions.

2.2 N doping by first-principle calculation

Total energies of N-doped $BaSi_2$ and their densities of states (DOSs) were calculated using the Vienna Ab initio Simulation Package code [36] based on density-functional theory with the projector-augmented wave pseudopotential [37] and Perdew-Wang Generalized Gradient Approximation method [38]. Total energy minimization was obtained via optimization of the lattice parameters and relaxation of the atomic positions in a conjugate gradient routine. Using an energy cutoff of 600 eV and a 6 × 8 × 4 grid of Monkhorst–Pack points, the convergence in the total energy was better than 1 meV/atom [39]. The stoichiometric description of the unit cell is Ba_8Si_{16}. In each $BaSi_2$ unit cell, there are two crystallographically inequivalent sites for Ba ($Ba^{(1)}$ and $Ba^{(2)}$) and three inequivalent sites for Si ($Si^{(3)}$, $Si^{(4)}$, and $Si^{(5)}$). Therefore the atoms are distributed over $4Ba^{(1)}$, $4Ba^{(2)}$, $4Si^{(3)}$, $4Si^{(4)}$, and $8Si^{(5)}$. Hereafter, we describe the N-doped $BaSi_2$ as $Ba_7N^{(1)}Si_{16}$, in which one of the $Ba^{(1)}$ sites is substituted with N, or $Ba_8N^{(3)}Si_{15}$, in which one of the $Si^{(3)}$ sites is substituted with N. There are 16 candidate interstitial sites in the $BaSi_2$ lattice. According to Imai and Watanabe [29], the most probable

insertion sites are the 4*c* sites, where an impurity atom is surrounded by three Si atoms, one located at a corner of one Si-tetrahedron and the other two composing an edge of the other Si-tetrahedron. Thus, we chose one of the 4*c* sites, the fractional coordinate of which is (0.5841, 0.25, 0.2251). This compound is described as $Ba_8Si_{16}N$. The calculated total energies of these compounds are summarized in Table 2. Energetic evaluation of possible interstitial compound formation of $BaSi_2$ was reported in ref. [40].

3. Results and discussion

The θ-2θ XRD patterns of samples B, E, F, and G are shown in Fig. 2. The values of I_N were varied as 611, 655, 780, and 1097 counts, respectively. The diffraction peaks of only (100)-oriented $BaSi_2$ and streaky RHEED patterns are observed at I_N = 611 (sample B) and 655 counts (sample E), indicating that N-doped $BaSi_2$ films were epitaxially grown. Similar results were obtained for samples A, C, and D. With increasing I_N, however, the spotty RHEED pattern appears in sample F. This means that the surface of N-doped $BaSi_2$ became rough. When the I_N is increased much further in sample G, the RHEED pattern becomes faint. The FWHM values obtained from an ω–scan x-ray rocking curve using a $BaSi_2$(600) diffraction peak are shown in Fig. 3. They are comparable to those of approximately 100 nm-thick undoped $BaSi_2$ [41] when the I_N is equal to 655 counts or smaller. When the I_N increases further to 780 counts in sample F, the FWHM becomes higher than 0.7 deg, meaning that the crystalline quality was degraded.

Figure 4 shows the SIMS depth profiles of N atoms in samples E and H. The plasma power was set differently. The N atom is almost homogeneously distributed throughout the grown layers regardless of plasma power. The N concentration is approximately 2×10^{20} cm^{-3}. Figure 5 shows the I_N dependences of carrier concentration and mobility of N-doped $BaSi_2$ measured at room temperature (RT). The electron concentration and the electron mobility of undoped n-$BaSi_2$ are approximately $2 \times 10^{16}cm^{-3}$ [42] and 820 cm^2/Vs [43], respectively. At

I_N equal to 655 counts or smaller, the N-doped $BaSi_2$ showed p-type conductivity, which differs from our prediction. The hole concentration was of the order of 10^{16}–10^{17} cm^{-3}, independently of I_N. The hole mobility was as small as tens of cm^2/Vs. This value is comparable to B-doped $BaSi_2$ [44]. On the other hand, when the I_N was equal to 780 counts or higher, N-doped $BaSi_2$ became an n-type semiconductor. Note here that the mobility jumped into more than 1000 cm^2/Vs. Such a high electron mobility can be expected for electrons flowing through the high-ρ FZ n-Si(111) substrate used in this work [45]. Due to a small electron affinity of $BaSi_2$ (3.2 eV) [46], the electron accumulation is likely to occur in the n-Si side near the n-$BaSi_2$/n-Si heterointerface if the N-doped $BaSi_2$ becomes an n-type semiconductor. We therefore can state that the electron concentrations shown in Fig. 5 were not correctly measured by the Hall measurement. Hence, we focus on the electrical properties of p-type $BaSi_2$ afterwards.

We next discuss the acceptor level E_A in p-$BaSi_2$. We fit the temperature dependence of the hole concentration, p, shown in Fig. 6(a) with Eq. (1).

$$p(T) = N_1 \exp\left(-\frac{E_A}{2k_B T}\right). \qquad (1)$$

Here, T is the absolute temperature, k_B is the Boltzmann constant, and N_1 is the density of level E_A. The obtained E_A and N_1 were approximately 64 meV and 5×10^{18} cm^{-3}, respectively. The value of 5×10^{18} cm^{-3} is approximately 40 times smaller than the N concentration (2×10^{20} cm^{-3}) in sample E, shown in Fig. 4. Hence, we speculate that most of the N atoms are not electrically active in the $BaSi_2$ probably because they exist in the form of N_2 molecules. Figure 6(b) shows the temperature dependence of hole mobility, μ. The mobility reached a maximum of 1025 cm^2/Vs at 60 K, and decreased with increasing temperature, indicating that the hole mobility was affected by lattice scattering. The inserted solid line is expressed by the relation $\mu \propto T^{-1.5}$. The conduction mechanism can be investigated from the temperature dependence of resistivity ρ. In general, at low temperatures, carriers in a system having

disorder caused by, for example, impurity doping are thought to hop from one impurity atom to the next, and the Coulomb potential around the impurity atom is overcome by means of thermal energy. The conductivity in such a system is determined by a hopping transport, where ρ has been found to follow the law,

$$\log\rho \propto \left(T^{*}/T\right)^{1/q}, \qquad (2)$$

where T^{*} is the characteristic temperature, and q is the parameter determining the Mott-type (q=2) or the Shklovskii-Efros (SE) type (q=4) variable-range hopping (VRH) conduction [47,48]. Figure 6(c) shows the logarithmic dependence of ρ on both $1/T^{1/2}$ and $1/T^{1/4}$ for N-doped $BaSi_2$, sample E. The linear behavior evident indicates that the carrier transport in the film can be explained by VRH conduction at lower temperatures. We cannot say for certain at present which of the SE-type or the Mott-type VRH conduction better describes the film properties. On the basis of these results, we conclude that VRH conductions occur in N-doped p-$BaSi_2$. The temperature dependence of resistivity in Ga-, Al-, Ag-, or Cu-doped $BaSi_2$ is also well explained by both Shklovskii-Efros-type and Mott-type VRH conduction [49].

We finally discuss the N site in the $BaSi_2$ lattice. It is hard to explain the p-type conductivity of N-doped $BaSi_2$. This is because the replacement of some Si atoms in $BaSi_2$ by N atoms increases the valence electron concentration and may cause $BaSi_2$ to become an n-type semiconductor. Table 2 summarizes the calculated total energies of $Ba_7N^{(1)}Si_{16}$, $Ba_8N^{(3)}Si_{15}$, and $Ba_8Si_{16}N$. The energy differences between $Ba_7N^{(1)}Si_{16}$ and $Ba_7N^{(2)}Si_{16}$ and between $Ba_8N^{(3)}Si_{15}$, $Ba_8N^{(4)}Si_{15}$, and $Ba_8N^{(5)}Si_{15}$ are small. Hence, we chose one $Ba^{(1)}$ site for Ba substitution, and one $Si^{(3)}$ site for Si substitution in this article although there are another Ba site, $Ba^{(2)}$, and the other two Si sites, $Si^{(4)}$ and $Si^{(5)}$, in Ba_8Si_{16}. The total energy after impurity doping is calculated using the binding energies of the optimized structures as follows: for one N atom replacing one Ba atom at the $Ba^{(1)}$ site, the total energy of $Ba_7N^{(1)}Si_{16}$

+ Ba is given by −132.188 − 1.912 = −134.100 eV. In the same way, the total energy of $Ba_8N^{(3)}Si_{15}$ and $Ba_8Si_{16}N$ are calculated to be −141.279 and −141.932 eV, respectively. From an energetic point of view, these results imply that the N atom is most likely to occupy the interstitial 4*c* site. Figure 7 shows the total DOSs of $Ba_7N^{(1)}Si_{16}$, $Ba_8N^{(3)}Si_{15}$, and $Ba_8Si_{16}N$, where their E_F's represent the energy zero. The E_F is located in the conduction band of $Ba_8N^{(3)}Si_{15}$ and there is no localized states within the band gap as shown in Fig. 7(b), suggesting that $Ba_8N^{(3)}Si_{15}$ is an n-type semiconductor as expected. In contract, localized states exist in the forbidden band gap above the valence band edge in $Ba_7N^{(1)}Si_{16}$ and $Ba_8Si_{16}N$, as shown in Fig. 7(a)(c), respectively. From the energetic point of view, $Ba_8Si_{16}N$ is mostly likely to occur in N-doped $BaSi_2$ as discussed above. We speculate that that's why the hopping transport occurs in N-doped p-$BaSi_2$. On the basis of these results, N is not a proper dopant for $BaSi_2$. Now that we have finished the investigation of availability of group 15 elements (N, P, As, and Sb) as a dopant for $BaSi_2$, we conclude that Sb or P is suitable for n-type $BaSi_2$.

4. Conclusion

We have grown N-doped $BaSi_2$ epitaxial films on high-resistivity n-type Si (111) substrates by MBE. N-doped $BaSi_2$ exhibited the n-type or p-type conductivity depending on the plasma intensity. The hole concentration was of the order of 10^{16}–10^{17} cm^{-3} at RT, and the acceptor level was approximately 64 meV from the temperature dependence of hole concentration. The hole transport was explained by the VRH conduction at low temperatures. First-principle calculations by VASP predicted that the N atom is mostly likely to occupy the interstitial 4*c* site rather than the substitutional site.

Acknowledgements

This work was supported in part by the Core Research for Evolutional Science and Technology (CREST) project of the Japan Science and Technology Agency (JST) and by a Grant-in-Aid for Scientific Research A (15H02237) from the Japan Society for the Promotion of Science (JSPS). R.T. was financially supported by a Grant-in-Aid for JSPS Fellows (15J02139).

References

[1] M. G. Panthani, V. Akhavan, B. Goodfellow, J. P. Schmidtke, L. Dunn, A. Dodabalapur, P. F. Barbara, B. A. Korgel, J. Am. Chem. Soc. **130** (2008) 16770.

[2] W. Jaegermann, A. Klein, T. Mayer, Adv. Mater. **21** (2009) 4196.

[3] S. Ahmed, K. B. Reuter, O. Gunawan, L. Guo, L. T. Romankiw, H. Deligianni, Adv. Ener. Mater. **2** (2012) 253.

[4] C. Steinhagen, M. G. Panthani, V. Akhavan, B. Goodfellow, B. Koo, B. A. Korgel, J. Am. Chem. Soc. **131** (2009) 12554.

[5] M. A. Green, A. Ho-Baillie, H. J. Snaith, Nature Photonics **8** (2014) 506.

[6] H. S. Kim, S. H. Im, N. G. Park, Journal of Physical Chemistry C **118** (2014) 5615.

[7] J. Evers, G. Oehlinger, A. Weiss, Angew. Chem. Int. Ed. Engl. **16** (1977) 659.

[8] M. Imai, T. Hirano, J. Alloys Compd. **224** (1995) 111.

[9] M. Baba, M. Kohyama, T. Suemasu, J. Appl. Phys. **120** (2016) 085311.

[10] T. Suemasu, Jpn. J. Appl. Phys. **54** (2015) 07JA01.

[11] T. Suemasu, N. Usami, J. Phys. D: Appl. Phys. **50** (2017) 023001

[12] D. Tsukahara, S. Yachi, H. Takeuchi, R. Takabe, W. Du, M. Baba, Y. Li, K. Toko, N. Usami, T. Suemasu, Appl. Phys. Lett. **108** (2016) 152101.

[13] S. Yachi, R. Takabe, K. Toko, T. Suemasu, Appl. Phys. Lett. **109** (2016) 072103.

[14] R. Takabe, S. Yachi, W. Du, D. Tsukahara, H. Takeuchi, K. Toko, T. Suemasu, AIP Advances **6** (2016) 085107.

[15] A. Pokhrel, L. Samad, F. Meng, S. Jin, Nanoscale **7** (2015) 17450.

[16] R. Vismara, O. Isabella, M. Zeman, Proc. SPIE **9898** (2016) 98980J.

[17] K. O. Hara, N. Usami, Y. Hoshi, Y. Shiraki, M. Suzuno, K. Toko, T. Suemasu, Jpn. J. Appl. Phys. **50** (2011) 121202.

[18] M. Ajmal Khan, K. Nakamura, W. Du, K. Toko, N. Usami, T. Suemasu, Appl. Phys. Lett. **104** (2014) 252104.

[19] M. Takeishi, Y. Matsumoto, R. Sasaki, T. Saito, T. Suemasu, Physics Procedia **11** (2011) 27.

[20] M. Kobayashi, Y. Matsumoto, Y. Ichikawa, D. Tsukada, T. Suemasu, Appl. Phys. Express **1** (2008) 051403.

[21] K. O. Hara, N. Usami, M. Baba, K. Toko, T. Suemasu, Thin Solid Films **567** (2014) 105.

[22] K. O. Hara, Y. Hoshi, N. Usami, Y. Shiraki, K. Nakamura, K. Toko, T. Suemasu, Thin Solid Films **557** (2014) 90.

[23] M. Baba, K. Ito, W. Du, T. Sanai, K. Okamoto, K. Toko, S. Ueda, Y. Imai, A. Kimura, T. Suemasu, J. Appl. Phys. **114** (2013) 123702.

[24] Y. Imai Y, A. Watanabe, M. Mukaida, J. Alloys Compd. **358** (2003) 257.

[25] L. I. Ivanenko, V. L. Shaposhnikov, A. B. Filonov, A. V. Krivosheev, V. E. Borisenko, D. B. Migas, K. Miglio, G. Behr, J. Schumann, Thin Solid Films **461** (2004) 141.

[26] D. B. Migas, V. L. Shaposhnikov, V. E. Borisenko, Phys. Status Solidi b **244** (2007) 2611.

[27] M. Kumar, N. Umezawa, M. Imai, Appl. Phys. Express **7** (2014) 071203

[28] M. Kumar, N. Umezawa, M. Imai, J. Appl. Phys.**115** (2014) 203718.

[29] Y. Imai, A. Watanabe, Intermetallics **15** (2007) 1291.

[30] Y. Tokumaru, H. Okushi, T. Masui, T. Abe, Jpn. J. Appl. Phys. **21** (1982) L443.

[31] K. Nauka, M.S. Goorsky, H.C. Gatos, J. Lagowski, Appl. Phys. Lett. **47** (1985) 1341.

[32] N. Fuma, K. Tashiro, K. Kakumoto, Y. Takano, Jpn. J. Appl. Phys. **35** (1996)1993.

[33] Y. Inomata, T. Nakamura, T. Suemasu, F. Hasegawa, Jpn. J. Appl. Phys. **43** (2004) L478.

[34] R. Takabe, H. Takeuchi, W. Du, K. Ito, K. Toko, S. Ueda, A. Kimura, T. Suemasu, J. Appl. Phys. **119** (2016) 165304.

[35] H. Okumura, H. Hamaguchi, T. Koizumi, K. Balakrishnan, Y. Ishida, M. Arita, S. Chichibu, H. Nakanishi, T. Nagatomo, S. Yoshida, J. Cryst. Growth **189–190** (1998) 390.

[36] G. Kresse and D. Joubert, Phys. Rev. B **59** (1999) 1758.

[37] P. E. Blöchl, Phys. Rev. B **50** (1994) 17953.

[38] J. P. Perdew, J. A. Chevary, S. H. Vosko, K. A. Jackson, M. R. Pederson, D. J. Singh, C. Fiolhais, Phys. Rev. B **46** (1992) 6671.

[39] H. J. Monkhorst, J. D. Pack, Phys. Rev. B **13** (1976) 5188.

[40] Y. Imai, M. Sohma, T. Suemasu, Jpn. J. Appl. Phys. **54** (2015) 07JE03.

[41] R. Takabe, K. Nakamura, M. Baba, W. Du, M. Ajmal Khan, K. Toko, M. Sasase, K. O. Hara, N. Usami, T. Suemasu, Jpn. J. Appl. Phys. **53** (2014) 04ER04.

[42] W. Du, M. Baba, K. Toko, K. O. Hara, K. Watanabe, T. Sekiguchi, N. Usami, T. Suemasu, J. Appl. Phys. **115** (2014) 223701.

[43] K. Morita, Y. Inomata, T. Sueamsu, Thin Solid Films **508** (2006) 363.

[44] M. Emha Bayu, Cham Thi Trinh, R. Takabe, S. Yachi, K. Toko, N. Usami, T. Suemasu, Jpn. J. Appl. Phys. **56** (2017) 05DB01.

[45] S. M. Sze, Physics of Semiconductor Devices 2nd ed. (Wiley, 1981) p. 29.

[46] T. Suemasu, K. Morita, M. Kobayashi, M. Saida, M. Sasaki, Jpn. J. Appl. Phys. **45** (2006) L519.

[47] A.L. Efros, B.I. Shklovskii, J. Phys. C8 (1975) L49.

[48] A.L. Efros, J. Phys. C: Solid State Phys. **9** (1976) 2021.

[49] M. Ajmal Khan, T. Saito, N. Nakamura, M. Baba, W. Du, K. Toh, K. Toko, T. Suemasu, Thin Solid Films **522** (2012) 95.

Figure captions

Fig. 1 Emission spectra of nitrogen plasma set at 50 and 70 W.

Fig. 2 Examples of θ-2θ XRD and RHEED patterns observed along the Si[$11\bar{2}$] azimuth of samples B, E, F, and G. The asterisk (*) indicates the diffraction of the substrate used.

Fig. 3 Plasma intensity dependence of FWHM values obtained from an ω–scan XRD rocking curve using a $BaSi_2$(600) diffraction peak intensity.

Fig.4 SIMS depth profiles of N atoms in samples E and H grown at 70 and 50 W, respectively.

Fig. 5 Plasma intensity dependences of carrier concentration and mobility measured at RT.

Fig. 6 (a) Arrhenius plot of hole concentration, (b) temperature dependence of hole mobility, and (c) logarithmic dependence of resistivity on $1/T^{1/2}$ and $1/T^{1/4}$. Solid line in (b) and dotted lines in (c) are a guide to the eyes.

Fig. 7 Total DOSs of (a) $Ba_7N^{(1)}Si_{16}$, (b) $Ba_8N^{(3)}Si_{15}$, and (c) $Ba_8Si_{16}N$.

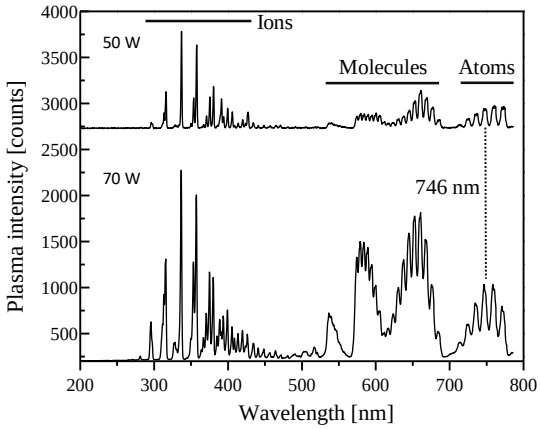
Ions
50 W
Molecules
Atoms
70 W
746 nm
Plasma intensity [counts]
Wavelength [nm]
4000
3500
3000
2500
2000
1500
1000
500
200
300
400
500
600
700
800

Fig. 1

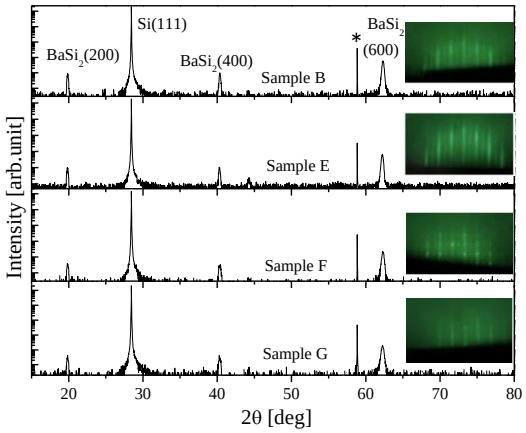
Si(111)
BaSi2(200)
BaSi2(400)
*
BaSi2
(600)
Sample B
Sample E
Sample F
Sample G
Intensity [arb.unit]
20
30
40
50
60
70
80
2θ [deg]

Fig. 2

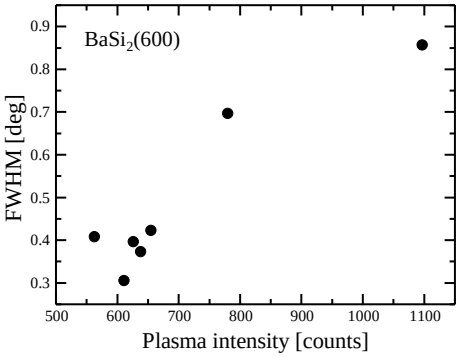
BaSi2(600)
FWHM [deg]
Plasma intensity [counts]
0.9
0.8
0.7
0.6
0.5
0.4
0.3
500
600
700
800
900
1000
1100

Fig. 3

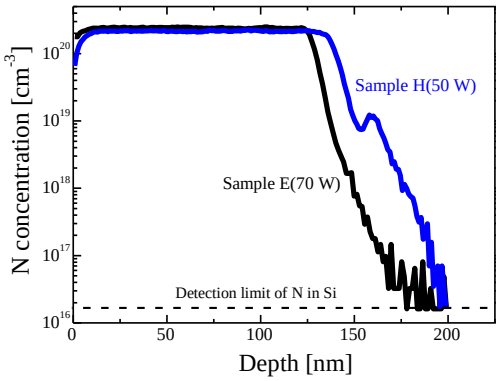
N concentration [cm^{-3}]
10^{20}
10^{19}
10^{18}
10^{17}
10^{16}
Sample H(50 W)
Sample E(70 W)
Detection limit of N in Si
0
50
100
150
200
Depth [nm]

Fig. 4

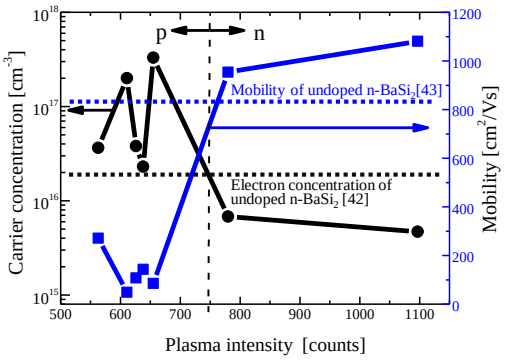
p
n
Mobility of undoped n-BaSi2[43]
Electron concentration of
undoped n-BaSi2 [42]
Carrier concentration [cm-3]
Mobility [cm2/Vs]
Plasma intensity [counts]

Fig. 5

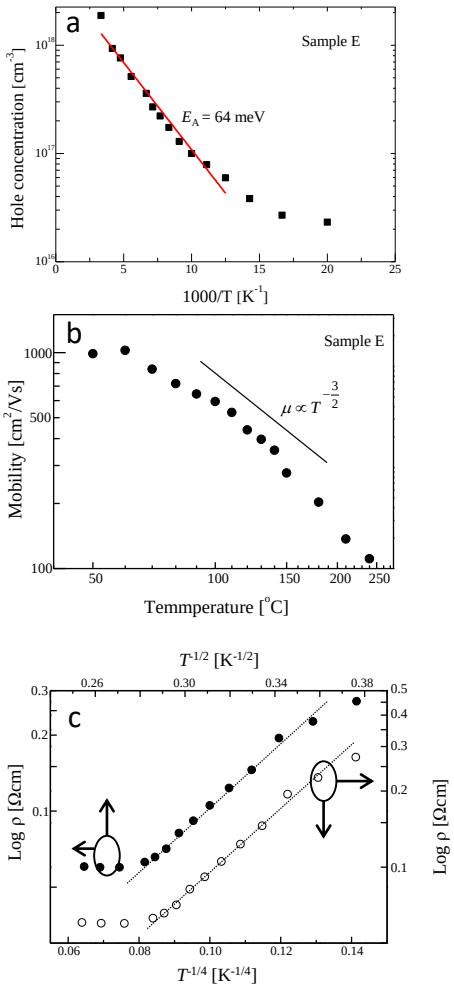
a
Sample E
E_A = 64 meV
Hole concentration [cm^{-3}]
1000/T [K^{-1}]
b
Sample E
$\mu \propto T^{-\frac{3}{2}}$
Mobility [cm^2/Vs]
Temmperature [^{o}C]
c
$T^{1/2}$ [K$^{-1/2}$]
Log ρ [Ωcm]
$T^{1/4}$ [K$^{-1/4}$]
Log ρ [Ωcm]

Fig. 6

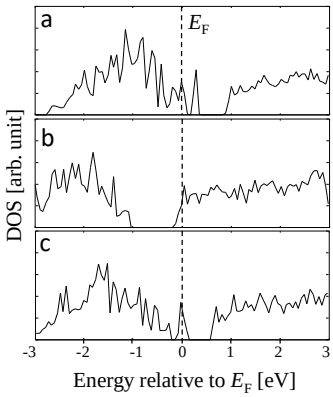

Fig. 7

Table 1 RF power, plasma intensity I_N, $BaSi_2$ layer thickness, and carrier concentration are indicated.

Sample	RF power (W)	I_N (counts)	Thickness (nm)	Carrier concentration (cm^{-3})
A	70	563	194	$p = 3.6 \times 10^{16}$
B	70	611	140	$p = 2 \times 10^{17}$
C	70	626	162	$p = 3.8 \times 10^{16}$
D	70	638	149	$p = 2.3 \times 10^{16}$
E	70	655	133	$p = 3.3 \times 10^{17}$
F	70	780	174	$n = 6.8 \times 10^{15}$
G	70	1097	172	$n = 4.7 \times 10^{15}$
H	50	421	218	$p = 3.9 \times 10^{15}$

Table 2. Calculated electronic energies for N-doped $BaSi_2$.

Compound	Total energy (eV)
$8Ba + 16Si \rightarrow Ba_8Si_{16}$	−133.696 [12]
	−134.100
$Ba_8Si_{16} + N \rightarrow Ba_7N^{(1)}Si_{16} + Ba$	(−132.188−1.912)
$Ba_8Si_{16} + N \rightarrow Ba_8N^{(3)}Si_{15} + Si$	−141.279
	(−135.862−5.417)
$Ba_8Si_{16} + N \rightarrow Ba_8Si_{16}N$	−141.932